

Fabrication of $p-n$ MoS₂/BiOBr heterojunction with few-layered structure for enhanced photocatalytic activity toward tetracycline degradation

Changyu Lu^{a,b}, Luning Gao^a, Shengju Yin^a, Feng Guo^c, Chuxuan Wang^b, Duo Li^{a,*}

^aSchool of Water Resources and Environment, Hebei Province Key Laboratory of Sustained Utilization and Development of Water Resources, Hebei Province Collaborative Innovation Center for Sustainable Utilization of Water Resources and Optimization of Industrial Structure, Hebei GEO University, Shijiazhuang 050031, P.R. China, Tel. +86 311 87208372; emails: Liduo556688@126.com (D. Li), pzpzlxl@163.com (C. Lu), gaoluning1997@163.com (L. Gao), y1179945009@163.com (S. Yin)

^bSchool of Geology and Environment, Xi'an University of Science and Technology, Xi'an, 710054, P.R. China, email: 422563710@qq.com

^cSchool of Energy and Power, Jiangsu University of Science and Technology, Zhenjiang, Jiangsu 212003, P.R. China, email: gfeng0105@126.com

Received 23 February 2020; Accepted 25 July 2020

ABSTRACT

The MoS₂/BiOBr heterojunction photocatalyst was successfully prepared by simple solvothermal process and used to remove tetracycline (TC) from water. The morphology, crystal structure, composition, and properties of the prepared samples were investigated by means of X-ray diffraction, scanning electron microscopy (SEM), Brunner–Emmet–Teller, UV-visible spectrophotometer, and X-ray photoelectron spectroscopy. SEM analysis showed that lamellar MoS₂ interspersed in the gap of BiOBr microspheres and formed spheroidal heterojunction structure. Among all the MoS₂/BiOBr with different mass ratios, 5 wt.% MoS₂/BiOBr displayed the highest photocatalytic activity, which can degrade 80.2% TC (40 mg/L) in 90 min and the rate constant is 0.01802 min⁻¹. It is 2.55 and 1.82 times higher than pure MoS₂ and BiOBr, respectively. It indicated the introduction of MoS₂ can not only promote the absorption band become broader, but also form the $p-n$ MoS₂/BiOBr heterojunction derives from the energy band matching and the formation of the built-in electric field which could improve the separation efficiency of photogenerated carriers. The study on photocatalytic mechanism by active species capturing and electron spin resonance experiments proved that h⁺ and •O₂⁻ were the predominant species in photocatalytic system. This research provides a strong practical support to construct highly efficient BiOBr-based $p-n$ heterojunction photocatalysts for photocatalytic applications of degradation on organic pollutants in aqueous environment.

Keywords: MoS₂/BiOBr; $p-n$ heterojunction; Photocatalysis; Tetracycline

1. Introduction

With the rapid development of economy and medical industry, antibiotics possessing the excellent antibacterial activity have been used extensively in human and livestock all over the world [1,2]. However, due to the unreasonable disposition and their un-metabolized forms through urine

and feces of users, antibiotics have been discharged into in surface water and groundwater and remain in the soil environment, which brought the potential pressure on the ecosystem balance and poses a great threat to human health [3,4]. Hence, extensive attention has been attracted on the removal of the broad-spectrum antibiotics from aqueous solution, and the development of a promising technology

* Corresponding author.

has become a priority. Semiconductor photocatalytic technology, as an advanced oxidation technology, can take advantage of the redox ability under illumination to achieve the purpose of purifying pollutants in aqueous solution, which has been regarded as an ideal, efficient, and environment-friendly purification craft [5–7].

As a semiconductor material with a band gap of around 2.50–2.91 eV, bismuth oxybromide (BiOBr) has attracted much attention due to its advantages in high efficiency, performed physical and chemical stability result from its layered structure formed by interlacing $[\text{Bi}_2\text{O}_2]$ and bromine atoms [8,9]. However, the photocatalytic performance of pristine BiOBr is confined by the poor quantum yield resulting from the high recombination rate of photogenerated electron–hole pairs [10]. Over the years, to make better use of BiOBr, various efforts have been carried out, such as morphology control [11], carbon material modification [12], noble metal modification [13] and heterojunction composite [14–16]. Theoretically, the construction of heterojunction composite photocatalyst is the simplest and effective method to suppress photo-generated carriers' recombination by steering the charge kinetics [17]. Notably, the BiOBr-based p – n heterojunction is favored because p -type semiconductor can be combined with n -type semiconductor and formed the built-in electric field in the composite, which can make the electrons and holes move in the opposite direction, thus effectively promoting the separation of photo-generated electrons and holes [18,19]. So far, BiOBr/BiOOCOOH [18], BiOBr/TiO₂ [19], and BiOBr/Bi₂MoO₆ [20] p – n heterojunctions have been proposed and it was confirmed that the photocatalytic effect of these heterojunctions was greatly improved compared to that of the pristine BiOBr. For example, Xu et al. [18] reported that the BiOBr/BiOOCOOH p – n heterojunction can efficiently improve electron–hole separation rate and exhibit much more accelerative degradation than pure samples under illumination of visible light. Wang et al. [19] decorated BiOBr nanosheets on TiO₂ nanofibers to form the hierarchical p – n heterojunctions for enhancing the degradation of RhB and MO under UV-light irradiation. Xue et al. [20] developed an effective Bi₂MoO₆/OV-BiOBr p – n heterojunction photocatalyst which significantly facilitated electron–hole pair separation and contributed to the adsorption and activation of inert N₂ molecules.

In our previous work, it has been proved that molybdenum disulfide (MoS₂) is an n -type semiconductor with layered structure, which can form p – n CuBi₂O₄/MoS₂ heterojunction with nanosheets-on-microrods structure for enhanced photocatalytic activity toward tetracycline degradation [21]. It is well known that MoS₂ is a transition metal sulfide and consists of hexagonal layers of Mo atoms sandwiched between two layers of S atoms with two-dimensional layered structure, which are superimposed by a weak van der Waals interaction [22,23]. In recent years, MoS₂ has been widely used as a photocatalytic material in the fields of organic pollutant degradation [24], photolysis of hydrogen [25], and carbon dioxide reduction [26]. Since MoS₂ has a narrow band gap of around 1.7 eV and has a strong absorption capacity in the visible region, which make MoS₂ have been used as a kind of cocatalyst to improve the photocatalytic activity of other semiconductors in recent years [27,28]. Wen et al. [29] synthesized

MoS₂/g-C₃N₄ nanocomposites showed enhanced visiblelight photocatalytic activity for the removal of nitric oxide (NO). To the best knowledge of the authors, some references on MoS₂/BiOBr composites photocatalysts have been already reported [30,31], but these investigations are mainly focusing on composites decrease the recombination of photo-generated charge carriers, the formation of p – n MoS₂/BiOBr heterojunction has not been reported yet. Thus, n -type MoS₂ were used as a co-catalyst couple p -type BiOBr to construct the p – n heterostructure composite to achieve full utilization of visible light and efficient separation of charge carriers, which effectively improved the photocatalytic photocatalytic degradation activity of organic pollutants.

In this work, a series of MoS₂/BiOBr p – n heterojunction photocatalysts were synthesized via a hydrothermal method. The crystal structure, microtopography, superficial chemical properties, and photochemical properties of the as-synthesized p – n heterojunction were characterized in detail. The photocatalytic quantification effect was determined by degrading the organic pollutant tetracycline (TC) under visible light ($\lambda > 420$ nm). Ultimately, based on the active species capturing experiment and electron spin resonance (ESR) results, the migration path of photogenerated charge carriers and the possible p – n heterojunction photocatalytic mechanism of MoS₂/BiOBr heterojunction composites were proposed.

2. Material

2.1. Synthesis of photocatalyst materials

1.25 mmol of sodium molybdate (Na₂MoO₄·2H₂O), 2.5 mmol of (CH₃CSNH₂) and 0.05 mmol of cetyltrimethyl ammonium bromide were successively added into 60 mL deionized water and stirred for 1 h. Then, the mixture solution was poured into a 100 mL Teflon-lined stainless steel autoclave heated at 180°C for 30 h. Afterwards, the product was cooled down to room temperature, washed several times with deionized water, and ethanol. Finally, the precipitate was dried in a vacuum drying oven at 60°C for 30 h to obtain purified MoS₂ powder.

For the MoS₂/BiOBr heterojunctions, different weight percentages MoS₂ were added to the fabricated process of BiOBr. 1 mmol of bismuth nitrate (Bi(NO₃)₃·5H₂O), 1 mmol of sodium bromide (NaBr) and a certain amount of MoS₂ prepared above were added into 20 mL of ethylene glycol (EG) solution and treated in the ultrasonic processor for 30 min. Then, the mixture solution was poured into a 50 mL Teflon-lined stainless steel autoclave heated at 160°C for 24 h. Afterwards, the obtained p – n MoS₂/BiOBr heterojunction was collected and washed several times with deionized water and ethanol, and dried at 70°C for 6 h. On this basis, different mass ratios of p – n MoS₂/BiOBr heterojunctions at 1, 3, 5, and 7 wt.% were prepared and denoted as MB-1%, MB-3%, MB-5%, and MB-7%, respectively.

2.2. Characterization of materials

The crystalline form and crystallinity of the obtained sample were analysed by powder X-ray diffraction (XRD, D8 Discover, Bruker) technique equipped with Cu-K α radiation

($\lambda = 0.154178$ nm). The microscopic morphology and the elements of the synthesized powder samples were analysed using an S-4800 scanning electron microscopy (SEM) instrument (Hitachi, Japan). The UV-vis absorption spectra were determined by UV-vis spectrophotometer (UV2550, Shimadzu, Japan) with barium sulphate as the reference. X-ray photoelectron spectroscopy (XPS) valence band spectra of the sample were determined by a K-Alpha XPS system (Thermo Fisher, USA) with Al K α irradiation as the excitation source and the C 1s binding energy of 284.6 eV as the internal standard. The Brunauer–Emmett–Teller (BET) surface area was determined from nitrogen adsorption–desorption isotherms at 77 K (ASAP2020, Micromeritics, Germany). The actual content of each element was carried out by the inductively coupled plasma emission spectrometer (ICP-AES) instrument (Icap6300, Thermo Fisher, USA). The photocurrent analysis was conducted in 0.5 M Na₂SO₄ electrolyte under 300 W Xe lamp irradiation. Electrochemical impedance spectroscopy (EIS) was recorded by using an alternating voltage of 5 mV amplitude in the frequency range of 10⁵–10² Hz with the open circuit voltage in 0.5 M Na₂SO₄.

2.3. Photocatalytic activity test

The visible light-induced photocatalytic performances of the as-synthesized samples were measured by degrading TC contaminated solution. In a typical reaction, a quantity of 25 mg of the catalyst was dispersed in 50 mL antibiotic solution (40 mg/L). Before photocatalytic degradation, the mixture solution was stirred for 30 min in dark to get the adsorption equilibrium. Then, a 300 W Xe lamp with a 420 nm cut-off filter was employed as the light source to trigger photocatalytic degradation reaction. The lamp-to-sample distance is 8 cm and the pH of the TC solutions is 6.8. The solution was magnetically stirred continuously, and a sample was collected every 15 min. After centrifugation, 3 mL supernatant was collected and analyzed by an UV-vis spectrophotometer at a maximum wavelength of 357 nm to determine the concentration of the aqueous solution. Total organic carbon (TOC) analysis was measured on a multi N/C2100 (Analytik Jena AG, Germany) TOC analyzer. The degradation rate of the TC solution was calculated by the following formula:

$$D = \left(1 - \frac{C_t}{C_0} \right) \times 100\% \quad (1)$$

where C_0 was the initial concentration of TC and C_t was the final concentration of TC after exposure.

2.4. Active species trapping tests

Sacrificial agents such as isopropanol (IPA), ethylenediamine tetraacetate (EDTA-2Na), and benzoquinone (BQ) were used to capture the hydroxyl radicals ($\cdot\text{OH}$), photo-generated holes (h^+), and superoxide anion radicals ($\cdot\text{O}_2^-$), respectively. The ESR signals were measured using a Bruker ER200-SRC spectrometer (Germany) to further detect the presence of $\cdot\text{OH}$ and $\cdot\text{O}_2^-$ radicals in the photocatalytic reaction system under 300 W xenon lamp irradiation.

3. Results and discussion

Fig. 1 illustrates the XRD patterns of all the as-synthesized samples. For pure BiOBr, it shows obvious characteristic diffraction peaks at 10.9°, 25.2°, 32.2°, 46.2°, and 57.1°, consistent with the (001), (101), (110), (200), and (212) crystal planes of BiOBr JCPDS No. 09-0393 [32]. The characteristic diffraction peaks of MoS₂ can perfectly indexed to JCPDS No. 37-1492 [33]. After the formation of MoS₂/BiOBr heterojunction, the characteristic diffraction peaks of MoS₂ do not appear. It may be due to the low content of MoS₂ and the sensitivity of the method [34]. In order to further prove the existence and actual content of MoS₂ in the composite sample, the ICP-AES element was carried out to analysis MB-5% sample. The test results are as shown in the Table 1, the actual element content ratio of Mo and Bi element is 1.00:38.70, and the actual mass content ratio of Mo and Bi element is 1.00:18.96 which is close to the stoichiometric ratio of 1.00:19.00 in the composite. This result is consistent with the theoretical value within the allowable error range.

SEM were carried out to observe the morphologies of as-prepared photocatalyst. In Fig. 2a, MoS₂ shows walnut shape nanospheres structure with diameter of 400–800 nm. From Fig. 2b, pure BiOBr possessed microspheres shapes with the diameter of approximately 1.5–2 μm , and the microsphere was composed of numerous nanosheets and have many voids on the surface. In Figs. 2c and d, after MoS₂ combined with BiOBr, the presence of MoS₂ does not change the overall morphology of BiOBr. The MoS₂/BiOBr microsphere gradually grow larger and the sheets are more densely packed and rough. The diameter of the composite photocatalyst is about 2–3 μm . The rough surface of microspheres can enlarge the surface areas and then enhance the photocatalytic activities of the photocatalysts.

The N₂ adsorption–desorption of the BiOBr, MoS₂, and MB-5% samples are shown in Fig. 3. The adsorption–desorption behaviors of all the samples were feasible and showed a slight hysteresis, conforming to the shape of type-IV isotherms. According to the International Union of

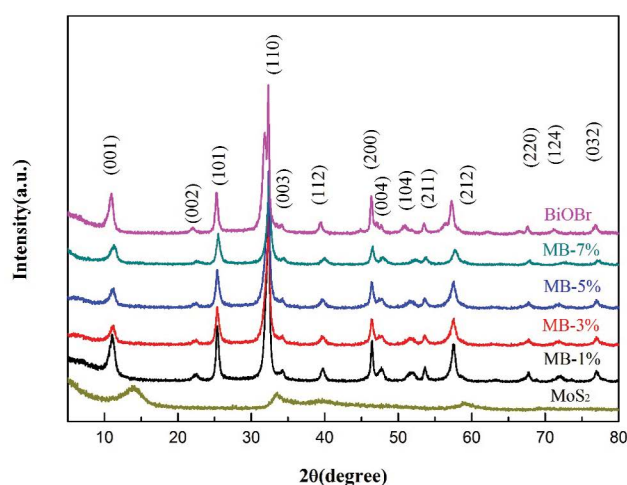


Fig. 1. XRD patterns of the as-synthesized MoS₂, BiOBr, and MoS₂/BiOBr samples.

Table 1
Theoretical and observed atom ratio of 7 MB-5% composite

| | Mo | Bi |
|-------------------------------------|--------------------------|---------------|
| Theoretical mass ratio | 1.00 (MoS ₂) | 19.00 (BiOBr) |
| Actual content concentration (mg/L) | 4.1 | 88.9 |
| Actual atomic ratio | 1.00 | 8.70 |
| Actual mass ratio | 1.00 (MoS ₂) | 18.96 (BiOBr) |

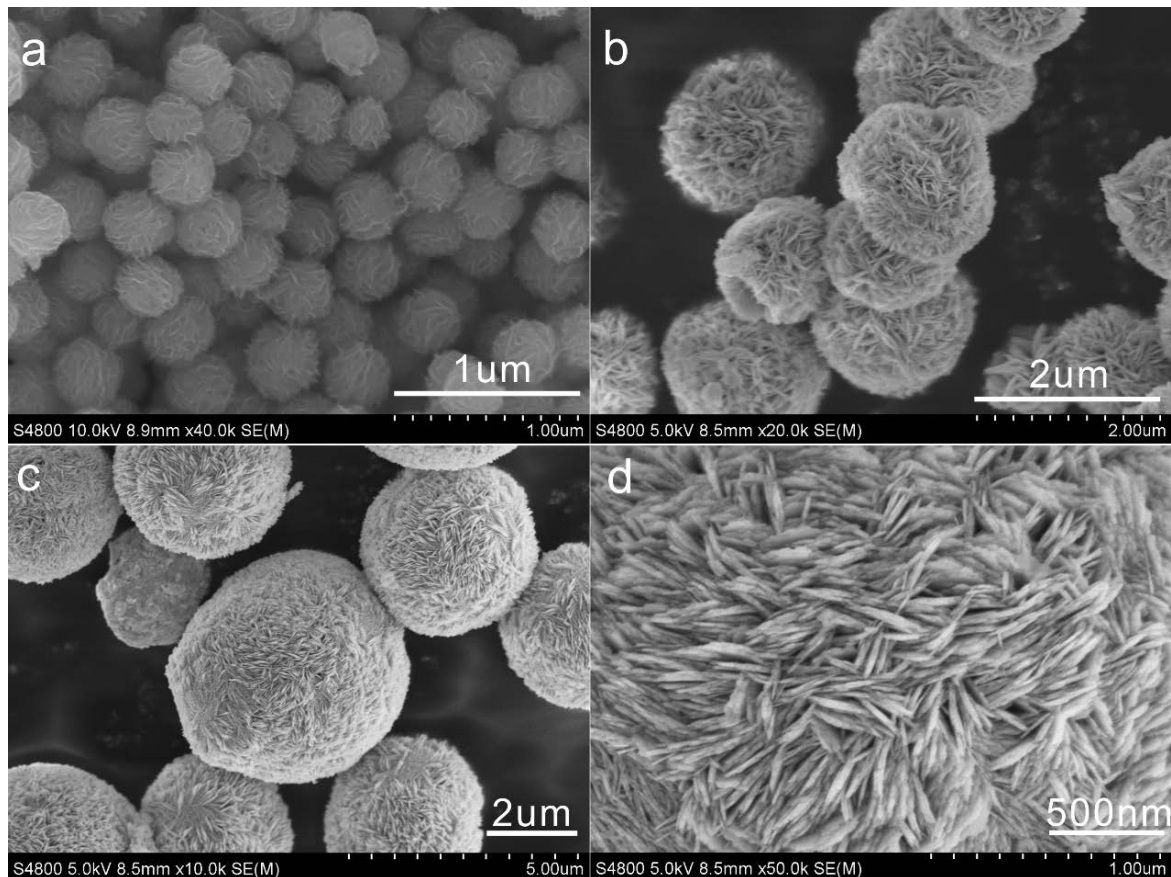


Fig. 2. SEM images of (a) MoS₂, (b) BiOBr, (c and d) MB-5% samples.

Pure and Applied Chemistry classification, all the samples have a *H3* hysteresis loop which confirm the presence of mesopores (2–50 nm) [35]. The specific surface area, pore area, and pore volume of the BiOBr, MoS₂, and MB-5% samples are presented on insert table. The pure MoS₂ sample has the largest specific surface areas, pore area, and pore volume. However, when MoS₂ is combined with BiOBr, the specific surface area and pore volume of MB-5% are slightly reduced. This is because the introduction of MoS₂ make spherical material becomes larger and the surface of microflowers composed of nanosheets becomes more compact. The rough surface of MB-5% microspheres can enhance the photocatalytic activities of the photocatalysts.

Fig. 4 shows the UV-visible diffuse reflection absorption spectrum of *p-n* MoS₂/BiOBr heterojunction photocatalyst. The absorption edge of the pure phase BiOBr is about

420 nm, and MoS₂ has a strong response respond to the whole visible light region due to its black feature and narrow band gap. After the introduction of MoS₂, MoS₂/BiOBr has slight red shift and the absorption intensity is enhanced in the visible light region. It indicates that the introduction of MoS₂ is beneficial to improve the light absorption of BiOBr. The E_g can be calculated by Tauc equation [36] as following:

$$\alpha h\nu = A[h\nu - E_g]^{n/2} \quad (2)$$

where α , h , ν , and A is absorption coefficient, Planck constant, light frequency, and a constant, respectively. For direct transition and indirect transition semiconductor, n equals 1 and 4, respectively. For MoS₂ and BiOBr, the n value both equal to 4 [21,37]. In Fig. 4b, according to Tauc

equation, the calculated band gaps of BiOBr and MoS₂ were 2.75 and 2.10 eV, respectively. The valence band (VB) and conduction band (CB) edge positions of MoS₂ and BiOBr were calculated by the following Eqs. (3) and (4) [38].

$$E_{\text{VB}} = \chi - E_e + 0.5E_g \quad (3)$$

$$E_{\text{CB}} = E_{\text{VB}} - E_g \quad (4)$$

where χ is the absolute electronegativity of the semiconductor (χ is 5.33 and 6.17 eV for MoS₂ and BiOBr, respectively), E_e is the energy of free electrons on the hydrogen scale (ca. 4.5 eV) and E_g is the band gap energy. Therefore, the E_{VB} of MoS₂ and BiOBr are calculated to be 1.88 and 2.21 eV (vs. NHE), respectively, by Eq. (1). According to Eq. (2), the E_{CB} of MoS₂ and BiOBr could be separately calculated to be -0.22 and -0.53 eV (vs. NHE).

The surface chemical composition and chemical status of elements in MB-5% can be analyzed in the XPS spectra.

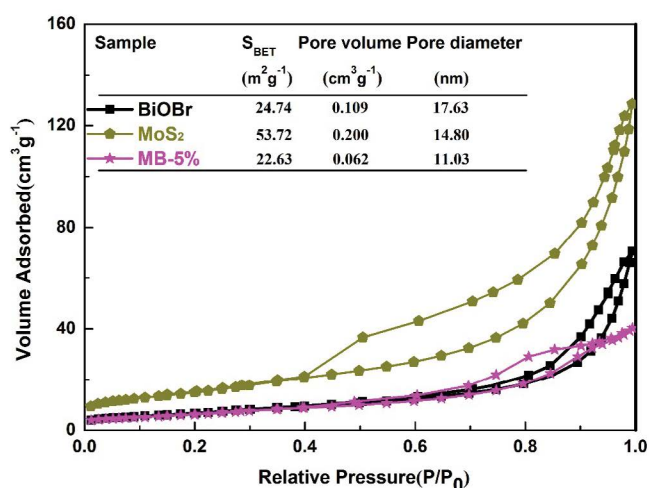
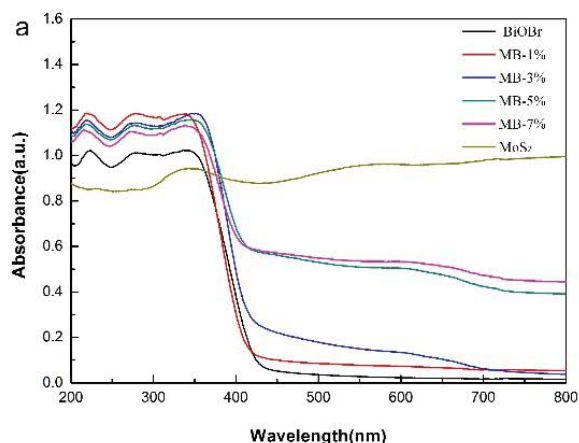


Fig. 3. (a) UV-vis diffuse reflection spectra of MoS₂, BiOBr, and MoS₂/BiOBr samples and (b) the plots of $(\alpha h\nu)^{1/2}$ vs. photo energy ($h\nu$) of MoS₂ and BiOBr.



In Fig. 5a, it can be seen that the composite mainly contains Br, Bi, Mo, and O. The Mo 3d XPS spectrum in Fig. 5b have two characteristic peaks at 227.7 and 233.3 eV are corresponding to Mo 3d_{5/2} and Mo 3d_{3/2}, indicating Mo exists as Mo⁴⁺ in MoS₂ [39]. While in Fig. 5b, two distinct characteristic peaks of MB-5% samples can be clearly seen at 164.9 and 159.7 eV, which correspond to the characteristic peaks of Bi 4f_{5/2} and Bi 4f_{7/2} [40]. With the formation of MoS₂/BiOBr heterojunction, the Bi 4f peaks exhibit a slight shift in comparison of pristine BiOBr materials. However, no obvious peak of S 2p spectrum were revealed, on one hand due to the low content of MoS₂ in the MB-5%, on the other hand, the peak positions of Bi 4f and S 2p are close and overlapped [41]. As displayed in Fig. 5d, the characteristic peak at 531.6 eV can be attributed to O 1s spectrum of MB-5% samples, demonstrating the presence of the crystal lattice oxygen (O²⁻) in the MB-5% [42]. Interestingly, the O 1s signal peak of MB-5% samples shifts to the lower binding energy in comparison of pristine BiOBr materials. Fig. 5e shows that the peak binding energy of 69.0 and 68.8 eV are assigned to Br 3d, which is characteristic of the Br⁻ in the MB-5% and BiOBr samples [43]. The XPS full spectra and high resolution analysis results of 5% MB-5% show that MoS₂ and BiOBr coexisted in the composite photocatalyst. The peaks of Bi 4f, O 1s, and Br 3d exhibit a slight shift in comparison of pristine BiOBr materials which imply the formation of MoS₂/BiOBr heterojunction [44].

To measure the photocatalytic performance of as-prepared *p-n* MoS₂/BiOBr heterojunction, tetracycline antibiotic wastewater was used as a degradation product and performed under simulated visible light with a 300 W Xe lamp. Fig. 6a shows that the dark absorption equilibrium is established after 30 min. The adsorption content of the composite photocatalysts is worse than that of MoS₂ and BiOBr, which is consistent with the results of BET presented in previous paragraph. As shown in Fig. 6b, the pristine MoS₂ and BiOBr exhibits the general photocatalytic performance, and the photocatalytic degradation efficiency of TC is 43.8% and 62.9% within 90 min, respectively. After the addition of MoS₂, the catalytic activity of the composite photocatalyst were enhanced obviously, suggesting that the combination of *p*-type BiOBr and *n*-type MoS₂ was a capable method to promote the photocatalytic performance by

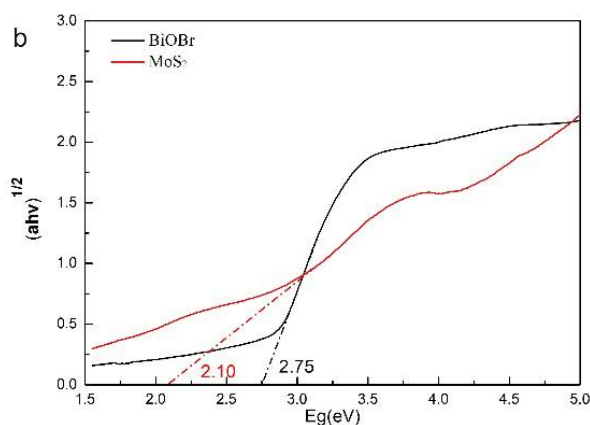


Fig. 4. (a and b) N₂ adsorption–desorption isotherms of MoS₂, BiOBr, and MB-5% samples.

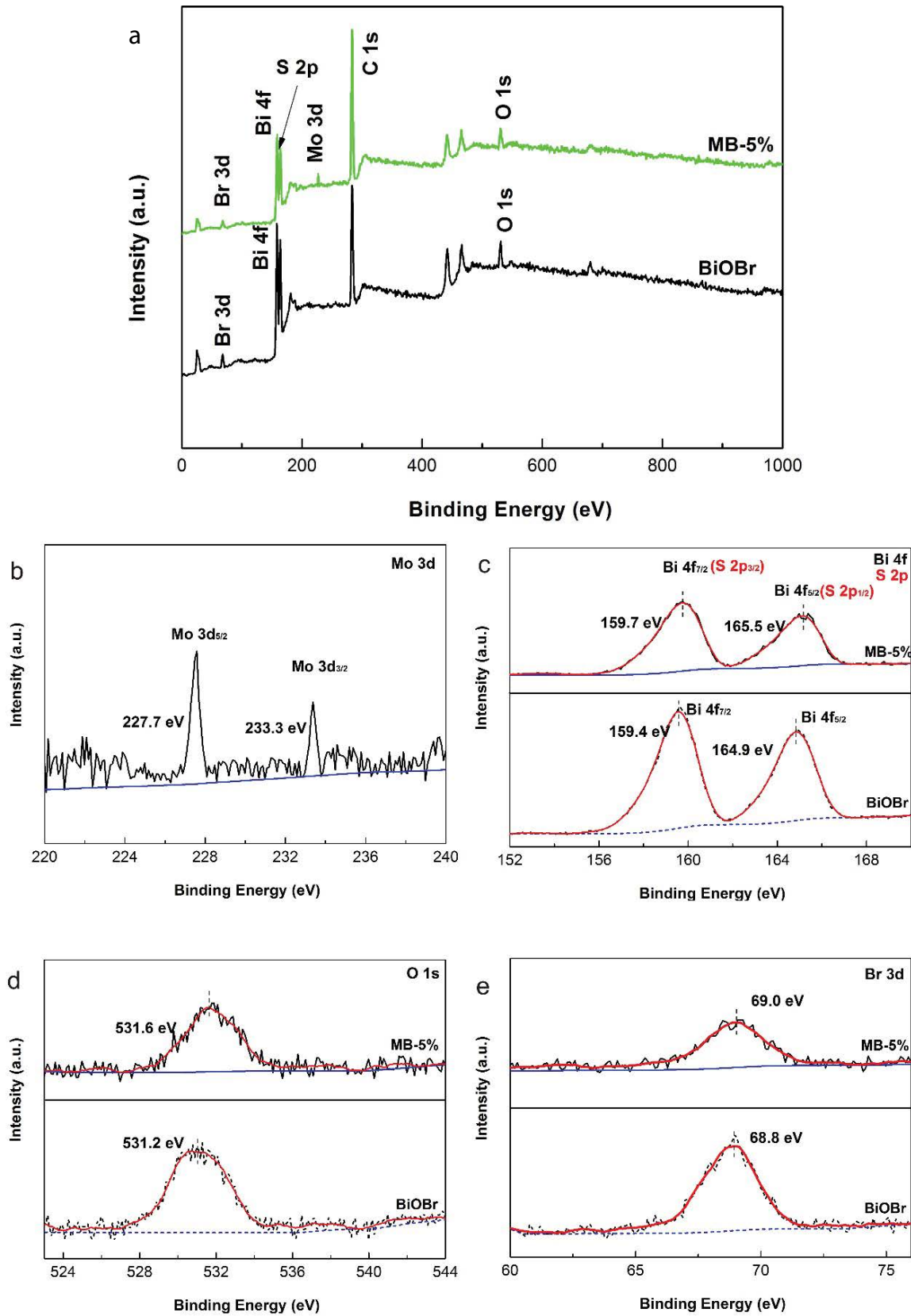


Fig. 5. (a) Full XPS survey and high-resolution XPS spectra of as-synthesized MB-5% heterojunction and BiOBr sample: (b) Mo 3d, (c) Bi 4f and S 2p, (d) O 1s, and (e) Br 3d.

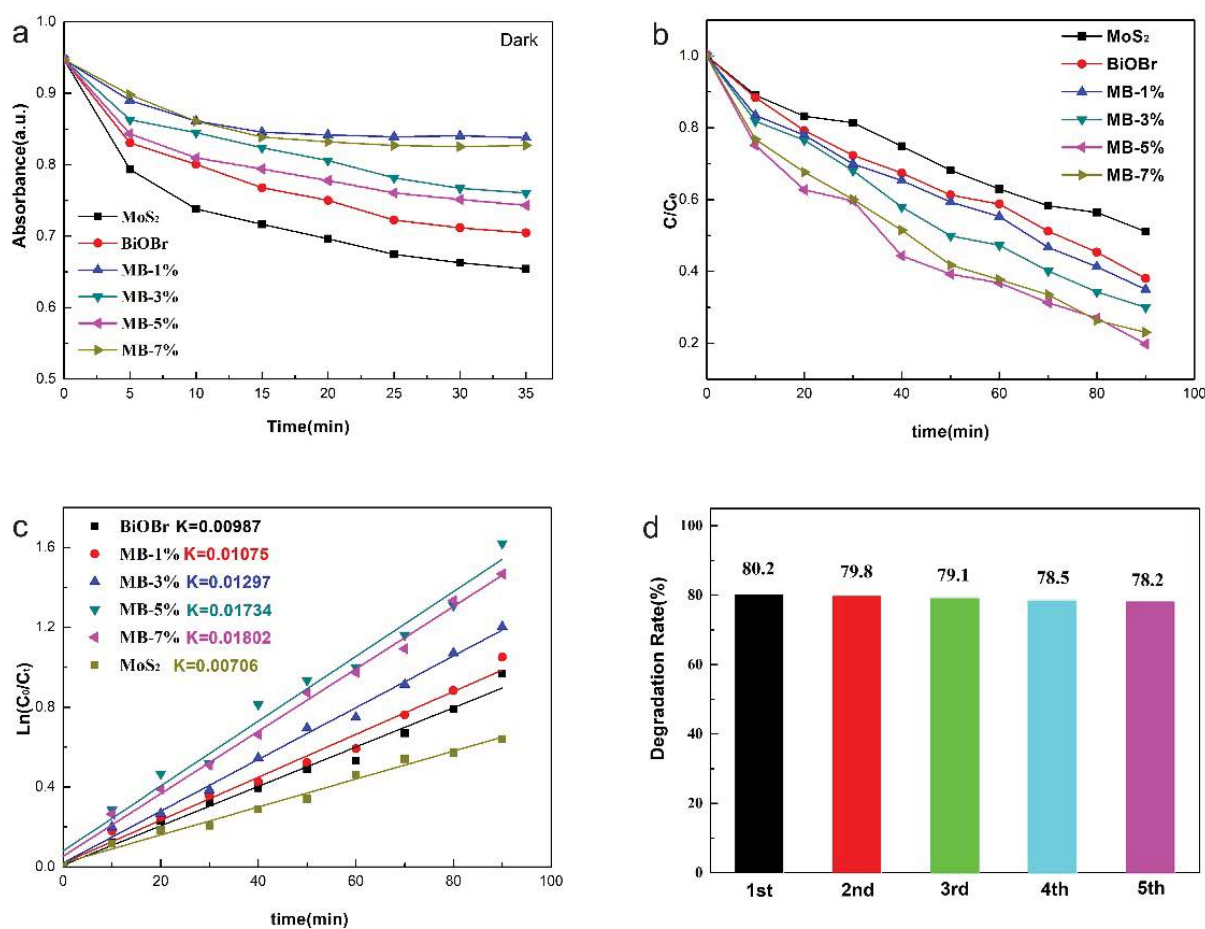


Fig. 6. (a) Absorption properties under dark conditions of TC over as-synthesized photocatalysts, (b) photocatalytic degradation of TC over as-synthesized photocatalysts under visible-light irradiation, (c) the apparent rate constants for TC degradation over the prepared samples, and (d) cycling runs for the photocatalytic degradation of TC in the presence of MB-5% sample.

p-n heterojunction. Meanwhile, the photocatalytic degradation efficiency of MB-1%, MB-3%, MB-5%, and MB-7% for MO are 65.1%, 69.9%, 80.2%, and 76.9%, respectively. Among them, MB-5% exhibits the optimum photocatalytic activity (90 min, 80.2%), which is around 1.83 and 1.28 times that of pristine MoS₂ and BiOBr, respectively. Nevertheless, after excessive addition of MoS₂ (exceeding 5 wt.%), the photocatalytic activity of the composite decreased. On one hand, the inappropriate ratio of MoS₂ will cover the effective reactive sites of the main catalyst BiOBr, which would decrease the specific area of the catalyst and lower its photocatalytic performance. On the another hand, the heterojunction will not generate due to the inappropriate ratio of MoS₂. 5%-MoS₂ modification on BiOBr will impact the charge transfer of the pure samples, which will inhibit the photo induced electron-hole separation efficiency of the composite. The corresponding pseudo-first-order kinetics plots and apparent rate constants of as-synthesized samples toward TC degradation were explicated in Fig. 6c. The *k*-values of photocatalytic degradation of TC over MB-1%, MB-3%, MB-5%, and MB-7% were 0.01075, 0.01297, 0.01734, and 0.01802 min⁻¹, respectively, which is much higher than the pure MoS₂ and BiOBr (0.00706 and 0.00987 min⁻¹).

It is well-known that the stability of photocatalyst is key to determine whether it can be put into practical application. Thus, the MB-5% sample was further chosen as the photocatalyst for the cycling experiment. As shown in Fig. 6d, the degradation rate was still over 90% of the initial degradation rate after five cycling runs, indicating the extraordinary stability and reusability of the MB-5% sample.

To verify the mineralization effect during the catalytic degradation of tetracycline, the TOC analysis was used to further determine the extent of tetracycline mineralization during photocatalysis. As illustrated in Fig. 7, the mineralization rate of samples with pure MoS₂ and BiOBr was 41% and 58% after 90 min irradiation under 300 W xenon lamp. While the removal rates of TOC of MB-1%, MB-3%, MB-5%, and MB-7% heterojunction photocatalyst were 62%, 68%, 71%, and 76%, respectively, which were slightly lower than those in the photocatalytic stage, but the TOC removal rate and photocatalytic degradation curves had similar trends. This result was reasonable, on the one hand, there are still a small amount of intermediates that are not completely converted into inorganic substances in the solution; on the other hand, the TOC data is obtained before radiometric test but the photocatalytic degradation result is data after

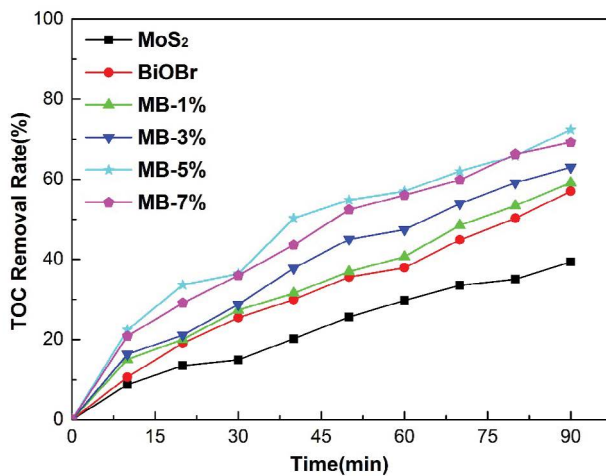
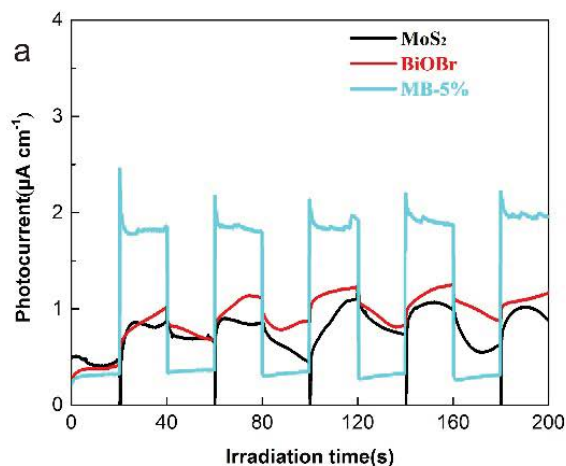


Fig. 7. TOC removal of TC over as-synthesized samples under visible-light irradiation.

centrifugation [45]. Moreover, widely environmental applications, such as the mineralization, would be implemented by $p-n$ $\text{MoS}_2/\text{BiOBr}$ heterojunction, since the reduced TOC contents suggested.

The enhanced separation efficiency of photogenerated electron-hole pairs by coupling BiOBr and MoS_2 was demonstrated using photocurrent, EIS. According to Fig. 8a, it was evident that both pure BiOBr and MoS_2 show lower photocurrent intensities due to the high recombination rate of photo-generated carriers. Notably, the photocurrent density increases after the formation of MB-5% sample. It is also proved that the MB-5% sample have the fastest transfer rate of photo-generated electrons and lead to more efficient separation of electron-hole pairs. EIS was also involved in exploring the charge-transfer impedance and photogenerated electron-hole pair transmission. MB-5% sample had the smallest radius, which further proves that $\text{MoS}_2/\text{BiOBr}$ heterojunction revealed accelerated interfacial charge migration rate, resulting in increased efficiency of the separation of photogenerated carriers.



To explore the main reactive species of $p-n$ $\text{MoS}_2/\text{BiOBr}$ heterojunction during the photocatalytic degradation of TC, IPA was used as hydroxyl scavenger, EDTA-2Na as hole trapping agent, and BQ as a superoxide radical trapping agent for the photocatalytic experiments [46]. As shown in the Fig. 9a, when no trapping agent was added to the system, the degradation rate of the MB-5% is still about 80% within 90 min. In contrast, when 1 mmol of EDTA-2Na and BQ were added to the system, the degradation rate of photocatalytic degradation of TC was significantly inhibited, indicating that $\cdot\text{O}_2^-$ and h^+ are the main active species in this system. When 1 mmol of IPA was added, the photocatalytic degradation efficiency of MB-5% heterojunction decreased from 80% to 63%, indicating that $\cdot\text{OH}$ is not the main active material in this photocatalytic reaction. To further verify the photocatalysis mechanism of $\text{MoS}_2/\text{BiOBr}$, ESR analysis was conducted to ensure the reactive species of trapping experiment. As shown in Fig. 9b, no ESR signals could be found under dark condition. However, the signal of DMPO- $\cdot\text{O}_2^-$ released from $\text{MoS}_2/\text{BiOBr}$ after xenon lamp irradiation was very obvious and the signal of DMOP- $\cdot\text{OH}$ is not obvious, which uncovers that $\cdot\text{O}_2^-$ can be generated and take part in the photocatalytic degradation reaction.

Based on the above data analysis, Fig. 10 show the possible photocatalytic mechanism of the $\text{MoS}_2/\text{BiOBr}$ heterojunction. Before the heterojunction is formed, the valence band (CB) and conduction band (VB) of MoS_2 and BiOBr are as shown in Fig. 10a. BiOBr and MoS_2 are nested band structures before the heterojunction are not formed between p -type BiOBr and n -type MoS_2 . In theory, a type II heterojunction can be formed. Under visible light illumination, both MoS_2 and BiOBr photogenerate electron-hole pairs. Electrons in the CB of BiOBr are accumulated in the CB of MoS_2 , while the holes in the VB of MoS_2 are accumulated to the VB of BiOBr. However, the CB potential of MoS_2 (-0.22 eV vs. NHE) is a little positive than the potential of $\text{O}_2/\cdot\text{O}_2^-$ (-0.33 eV vs. NHE), which implies that O_2 can be reduced to it is difficult to generate $\cdot\text{O}_2^-$ and separate the electrons and the holes in such structures [31]. Since the Fermi level of the p -type BiOBr semiconductor is close to its valence band, while the Fermi level of the n -type MoS_2 semiconductor is close to its

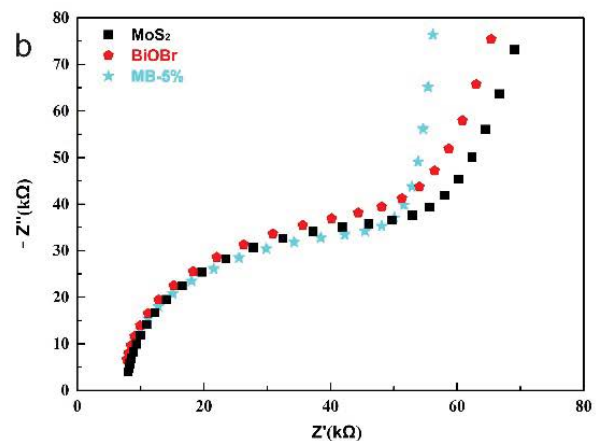


Fig. 8. (a) Photocurrent responses and (b) EIS Nyquist plot of as-synthesized photocatalysts.

conduction band, it is obvious that the Fermi level of MoS_2 is higher than that of BiOBr . When p -type BiOBr recombines with n -type MoS_2 and forms the p - n junction, in order to balance the Fermi energy, the charge will be redistribution, and the electrons will move from n -type MoS_2 to p -type BiOBr , while the holes flow toward the opposite direction [21]. As a result, MoS_2 becomes a positively charged impurity ion due to the loss of a part of electrons, and BiOBr becomes a negatively charged impurity ion due to the loss of holes. At this time, a space charge region is formed at the interface of the p - n junction, that is, a built-in electric field is formed. Under the action of this field, the Fermi level of MoS_2 moves down and the Fermi level of BiOBr moves up. When they achieve balance, the p - n junction is in equilibrium and the charges stop spreading. Meanwhile the band positions of MoS_2 and

BiOBr will be varied along with the change of Fermi levels. As shown in Fig. 10b, under visible light irradiation, both MoS_2 and BiOBr can produce photoexcited electrons and will jump from their VBs to CBs, leaving holes in VBs. In this way, through the establishment of the internal electric field at the $\text{MoS}_2/\text{BiOBr}$ p - n heterojunction interface, the photogenerated electrons can easily transfer at CB of BiOBr and MoS_2 , and the holes can transfer from the VB of MoS_2 to BiOBr , leading to effectively suppressed recombination of photogenerated carriers. Thereafter, the photogenerated electrons react with adsorbed oxygen and water molecules on the surface of the nanocomposite to produce reactive species of $\cdot\text{O}_2^-$ to degrade the TC, while the holes in VB of BiOBr can directly oxidize antibiotics to form the corresponding degradation products. The process was described as follows:

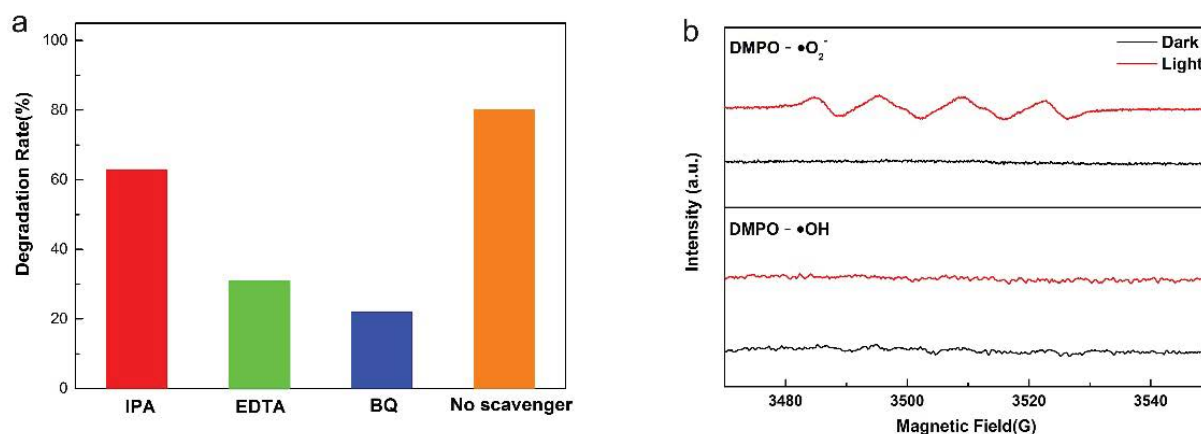


Fig. 9. (a) Trapping experiments of active species during the photocatalytic degradation of TC over MB-5% photocatalyst under visible light irradiation and (b) ESR spectra of MB-5% under dark and simulated solar light: $\text{DMPO}\cdot\text{O}_2^-$ in methanol dispersions and $\text{DMPO}\cdot\text{OH}$ in aqueous dispersions.

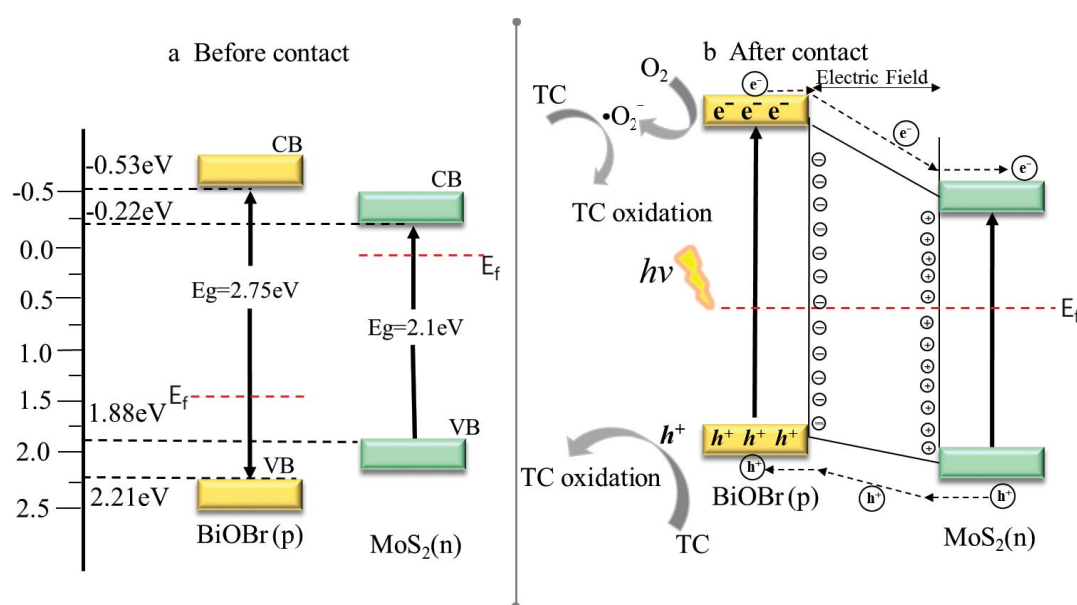
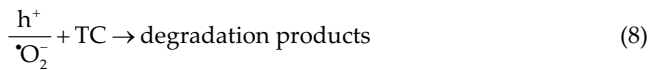
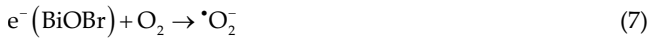
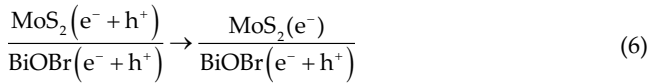
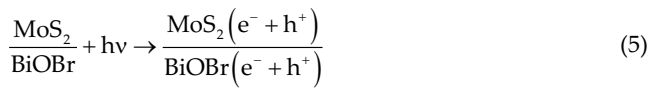


Fig. 10. Schematic of charge transfer between p -type BiOBr and n -type MoS_2 : (a) before contact and (b) after the formation of the p - n heterojunction.



4. Conclusions

In this study, the few-layered structured *p-n* MoS₂/BiOBr heterojunction with was synthesized through a facile solvothermal method. The crystal structure, micromorphology, surface physicochemical properties, photoelectrochemical properties, as well as the charge carriers transfer mechanism of the *p-n* heterojunction materials have been studied in detail. The MB-5% *p-n* heterojunction photocatalyst exhibits the outstanding photocatalytic performance in photocatalytic degradation of TC, which can be benefit from the inner electric field existence in the MoS₂/BiOBr *p-n* heterojunction could expedite the separation and migration of photogenerated carriers. Finally, the photocatalytic reaction mechanism over MoS₂/BiOBr *p-n* heterojunction was also uncovered in detail by the active species trapping experiments and ESR technique. The results in our research provides some new ideas and practical support for the rational fabrication of *p-n* heterojunction photocatalyst with superior photocatalytic activity and will be of great importance for water purification.

Acknowledgments

This work is supported by the National Natural Science Foundation of China (21906039, 21906072), Natural Science Foundation of Shaanxi Province (2019JQ-382), Funding project for introduced overseas scholars of Hebei Province (C20190321), Fundamental Research Funds for the Central Universities of Chang'an University (300102290501), Program for water resources research and promotion of Hebei Province (2019-55), and Doctoral research fund of Hebei Geo University (BQ2019041).

References

- [1] S. Ahmadi, A. Banach, F. Kord Mostafapour, D. Balarak, Study survey of cupric oxide nanoparticles in removal efficiency of ciprofloxacin antibiotic from aqueous solution: adsorption isotherm study, *Desal. Water Treat.*, 89 (2017) 297–303.
- [2] Q.W. Bu, B. Wang, J. Huang, S.B. Deng, G. Yu, Pharmaceuticals and personal care products in the aquatic environment in China: a review, *J. Hazard. Mater.*, 262 (2013) 189–211.
- [3] Q. Zhu, Y.K. Sun, F.S. Na, J. Wei, S. Xu, Y.L. Li, F. Guo, Fabrication of CdS/titanium-oxo-cluster nanocomposites based on a Ti₃₂ framework with enhanced photocatalytic activity for tetracycline hydrochloride degradation under visible hydrochloride, *Appl. Catal., B*, 254 (2019) 541–550.
- [4] Y.H. Zhou, P.Y. Li, M.J. Chen, Z.H. Dong, C.Y. Lu, Groundwater quality for potable and irrigation uses and associated health risk in southern part of Gu'an County, North China Plain, *Environ. Geochem. Health*, (2020), <https://link.springer.com/article/10.1007/s10653-020-00553-y>.
- [5] S.W. Tao, Y. Chen, J.W. Cui, H.W. Zhou, N. Yu, X.R. Gao, S.T. Cui, C. Yuan, M.Q. Liu, M.M. Wang, X.J. Wang, H.Y. Gong, Y.M. Li, T. Liu, X. Sun, J. Yin, X.X. Zhang, M.X. Wu, Organic-inorganic hybrid (CH₃NH₂)₂FeCuI₄Cl₂ and (CH₃NH₂)₂InCuI₄ for ultraviolet light photodetectors, *Chem. Commun.*, 56 (2020) 1875–1878.
- [6] C.Y. Lu, J.J. Dang, C.T. Hou, Y.J. Jiang, W.S. Guan, Photocatalytic degradation of doxycycline on ellipsoid-like BiVO₄ synthesized by EDTA-assisted, *Desal. Water Treat.*, 104 (2018) 250–256.
- [7] W.L. Shi, M.Y. Li, X.L. Huang, H.J. Ren, F. Guo, Y.B. Tang, C.Y. Lu, Construction of CuBi₂O₄/Bi₂MoO₆ *p-n* heterojunction with nanosheets-on-micro-rods structure for improved photocatalytic activity towards broad-spectrum antibiotics degradation, *Chem. Eng. J.*, 394 (2020) 125009–125018.
- [8] Y.J. Xing, Z.L. He, W.X. Que, Synthesis and characterization of ZnO nanospheres sensitized BiOBr plates with enhanced photocatalytic performances, *Mater. Lett.*, 182 (2019) 210–213.
- [9] B. Chai, J. Yan, G. Fan, G. Song, C. Wang, *In-situ* construction of Bi₂SiO₅/BiOBr heterojunction with significantly improved photocatalytic activity under visible light, *J. Alloys Compd.*, 802 (2019) 301–309.
- [10] X. Ren, K. Wu, Z. Qin, X. Zhao, H. Yang, The construction of type II heterojunction of Bi₂WO₆/BiOBr photocatalyst with improved photocatalytic performance, *J. Alloys Compd.*, 788 (2019) 102–109.
- [11] S.T. Navale, Q. Huang, P. Cao, V.B. Patil, F.J. Stadler, C₂H₅OH sensing properties of solid-state mediated BiOBr nanoplates, *Sens. Actuators, B*, 300 (2019) 122137–122147.
- [12] L. Allagui, B. Chouchene, T. Gries, G. Medjahdi, E. Giro, X. Framboisier, A.B.H. Amara, L. Balan, R. Schneider, Core/shell rGO/BiOBr particles with visible photocatalytic activity towards water pollutants, *Appl. Surf. Sci.*, 490 (2019) 580–591.
- [13] J.X. Guo, D.Y.S. Yan, F.L.Y. Lam, B.J. Deka, X.C. Lv, Y.H. Ng, A.K. An, Self-cleaning BiOBr/Ag photocatalytic membrane for membrane regeneration under visible light in membrane distillation, *Chem. Eng. J.*, 378 (2019) 126987–126996.
- [14] S.J. Zhang, X.X. Chen, L.M. Song, Preparation of BiF₃/BiOBr heterojunctions from microwave-assisted method and photocatalytic performances, *J. Hazard. Mater.*, 367 (2019) 304–315.
- [15] A. Khampuanbut, S. Santalelat, A. Pankiew, D. Channei, S. Pornsuwan, K. Faungnawakij, S. Phanichphant, B. Inceesungvorn, Visible-light-driven WO₃/BiOBr heterojunction photocatalysts for oxidative coupling of amines to imines: energy band alignment and mechanistic insight, *J. Colloid Interface Sci.*, 560 (2020) 213–224.
- [16] J. Yin, F. Di, J. Guo, K. Zhang, W. Xu, Y. Wang, S. Shi, N. Chai, C. Chu, J. Wei, W. Li, X. Shao, X. Pu, D. Zhang, X. Ren, J. Wang, J. Zhao, X. Zhang, X. Wei, F. Wang, H.W. Zhou, Tuning Ni-Foam into NiOOH/FeOOH heterostructures toward superior water oxidation catalyst via three-step strategy, *ACS Omega*, 3 (2018) 11009–11017.
- [17] X.Z. Yue, S.S. Yi, R.W. Wang, Z.T. Zhang, S.L. Qiu, Well-controlled SrTiO₃@Mo₃C core-shell nanofiber photocatalyst: boosted photo-generated charge carriers transportation and enhanced catalytic performance for water reduction, *Nano Energy*, 47 (2018) 463–473.
- [18] J.I. Xu, Y.K. Wang, J.F. Niu, M.D. Chen, Facile construction of BiOBr/BiOOH *p-n* heterojunction photocatalysts with improved visible-light-driven photocatalytic performance, *Sep. Purif. Technol.*, 225 (2019) 24–32.
- [19] K.X. Wang, Y.S. Zhang, L. Liu, N. Lu, Z. Zhang, BiOBr nanosheets-decorated TiO₂ nanofibers as hierarchical *p-n* heterojunctions photocatalysts for pollutant degradation, *J. Mater. Sci.*, 54 (2019) 8426–8435.

- [20] X.L. Xue, R.P. Chen, C.Z. Yan, Y. Hu, W.J. Zhang, S.Y. Yang, L.B. Ma, G.Y. Zhu, Z. Jin, Efficient photocatalytic nitrogen fixation under ambient conditions enabled by the heterojunctions of *n*-type Bi₂MoO₆ and oxygen-vacancy-rich *p*-type BiOBr, *Nanoscale*, 11 (2019) 10439–10445.
- [21] F. Guo, M.Y. Li, H.J. Ren, X.L. Huang, W.X. Hou, C. Wang, W.L. Shi, C.Y. Lu, Fabrication of *p*-*n* CuBi₂O₄/MoS₂ heterojunction with nanosheets-on-microspheres structure for enhanced photocatalytic activity towards tetracycline degradation, *Appl. Surf. Sci.*, 491 (2019) 88–94.
- [22] M. Xu, T. Liang, M. Shi, H. Chen, Graphene-like two-dimensional materials, *Chem. Rev.*, 113 (2013) 3766–3798.
- [23] H.W. Zhou, J.X. Guo, C. Wang, X.J. Liu, S.Z. Shi, J.Z. Wei, X.P. Pu, W.Z. Li, D.F. Zhang, J. Wang, X.Z. Ren, H.Y. Ma, X. Shao, X.T. Wei, J.S. Zhao, L. Yin, X.X. Zhang, 2D Schottky Junction between graphene oxide and transition-metal dichalcogenides: photoresponsive properties and electrocatalytic performance, *Adv. Mater. Interfaces*, 6 (2019) 1801657–1801662.
- [24] H.Y. Bai, W.Q. Fan, Y.L. Ge, P. Guan, W.D. Shi, One-step syntheses of MoS₂/graphitic carbon composites with enhanced photocatalytic activity under visible light irradiation, *New J. Chem.*, 41 (2017) 14171–14178.
- [25] Y. Liu, H.T. Niu, W. Gu, X.Y. Cai, B.D. Mao, D. Li, W.D. Shi, *In-situ* construction of hierarchical CdS/MoS₂ microboxes for enhanced visible-light photocatalytic H₂ production, *Chem. Eng. J.*, 339 (2018) 117–124.
- [26] B. Khan, F. Raziq, M.B. Faheem, M.U. Farooq, S. Hussain, F. Ali, A. Ullah, A. Mavlonov, Y. Zhao, Z.R. Liu, H. Tian, H.H. Shen, A.T. Zu, S. Li, H.Y. Xiao, X. Xiang, L. Qiao, Electronic and nanostructure engineering of bifunctional MoS₂ towards exceptional visible-light photocatalytic CO₂ reduction and pollutant degradation, *J. Hazard. Mater.*, 381 (2020) 120972–120981.
- [27] I. Song, C. Park, H.C. Choi, Synthesis and properties of molybdenum disulfide: from bulk to atomic layers, *RSC Adv.*, 5 (2015) 7495–7514.
- [28] J. Sun, L.X. Duan, Q. Wu, W. Yao, Synthesis of MoS₂ quantum dots cocatalysts and their efficient photocatalytic performance for hydrogen evolution, *Chem. Eng. J.*, 332 (2018) 449–455.
- [29] M.Q. Wen, T. Xiong, Z.G. Zang, W. Wei, X.S. Tang, F. Dong, Synthesis of MoS₂/gC₃N₄ nanocomposites with enhanced visible-light photocatalytic activity for the removal of nitric oxide (NO), *Opt. Express*, 24 (2016) 10205–10212.
- [30] J. Di, J.X. Xia, Y.P. Ge, L. Xu, H. Xu, J. Chen, M.Q. He, H. Li, Facile fabrication and enhanced visible light photocatalytic activity of few-layer MoS₂ coupled BiOBr microspheres, *Dalton Trans.*, 43 (2014) 15429–15438.
- [31] J.X. Xia, Y.P. Ge, D.X. Zhao, J. Di, M.X. Ji, S. Yin, H.M. Li, R. Chen, Microwave-assisted synthesis of few-layered MoS₂/BiOBr hollow microspheres with superior visible-light-response photocatalytic activity for ciprofloxacin removal, *CrystEngComm*, 17 (2015) 3645–3651.
- [32] J.L. Zhang, L.S. Zhang, X.F. Shen, P.F. Xu, J.S. Liu, Synthesis of BiOBr/WO₃ *p*-*n* heterojunctions with enhanced visible light photocatalytic activity, *CrystEngComm*, 18 (2016) 3856–3865.
- [33] G. Huang, T. Chen, W. Chen, Z. Wang, K. Chang, L. Ma, F. Huang, D. Chen, J.Y. Lee, Graphene-like MoS₂/graphene composites: cationic surfactant-assisted hydrothermal synthesis and electrochemical reversible storage of lithium, *Small*, 9 (2013) 3693–3703.
- [34] G.P. Chen, D.M. Li, F. Li, Y.Z. Fan, H.F. Zhao, Y.H. Luo, R.C. Yu, Q. Meng, Ball-milling combined calcination synthesis of MoS₂/CdS photocatalysts for high photocatalytic H₂ evolution activity under visible light irradiation, *Appl. Catal., B*, 443 (2012) 138–144.
- [35] A. Grosman, C. Ortega, Capillary condensation in porous materials. Hysteresis and interaction mechanism without pore blocking/percolation process, *Langmuir*, 24 (2008) 3977–3986.
- [36] J.F. Guo, P.T. Li, Z.Y. Yang, A novel Z-scheme g-C₃N₄/LaCoO₃ heterojunction with enhanced photocatalytic activity in degradation of tetracycline hydrochloride, *Catal. Commun.*, 122 (2019) 63–67.
- [37] J. Chen, M. Guan, W.Z. Cai, J.J. Guo, C. Xiao, G. Zhang, The dominant {001} facet-dependent enhanced visible-light photoactivity of ultrathin BiOBr nanosheets, *Phys. Chem. Chem. Phys.*, 16 (2014) 20909–20914.
- [38] M.A. Butler, D.S. Ginley, Prediction of flatband potentials at semiconductor-electrolyte interfaces from atomic electronegativities, *J. Electrochem. Soc.*, 125 (1978) 228–232.
- [39] R.Q. Ye, P. del Angel-Vicente, Y.Y. Liu, M.J. Arellano-Jimenez, Z.W. Peng, T. Wang, Y.L. Li, B.I. Yakobson, S.H. Wei, M.J. Yacaman, J.M. Tour, High-performance hydrogen evolution from MoS_{2(1-x)} Px solid solution, *Adv. Mater.*, 28 (2016) 1427–1432.
- [40] Y.C. Feng, L. Li, J.W. Li, J.F. Wang, L. Liu, Synthesis of mesoporous BiOBr 3D microspheres and their photodecomposition for toluene, *J. Hazard. Mater.*, 192 (2011) 538–544.
- [41] C.Y. Lu, F. Guo, Q.Z. Yan, Z.J. Zhang, D. Li, L.P. Wang, Y.H. Zhou, Hydrothermal synthesis of type II ZnIn₂S₄/BiPO₄ heterojunction photocatalyst with dandelion-like microflower structure for enhanced photocatalytic degradation of tetracycline under simulated solar light, *J. Alloys Compd.*, 811 (2019) 151976–151982.
- [42] W.L. Shi, F. Guo, M.Y. Li, Y. Shi, M.J. Shi, C. Yan, Constructing 3D sub-micrometer CoO octahedrons packed with layered MoS₂ shell for boosting photocatalytic overall water splitting activity, *Appl. Surf. Sci.*, 473 (2019) 928–933.
- [43] L.Q. Ye, X.L. Jin, C. Liu, C.H. Ding, H.Q. Xie, K.H. Chu, P.K. Wong, Thickness-ultrathin and bismuth-rich strategies for BiOBr to enhance photoreduction of CO₂ into solar fuels, *Appl. Catal., B*, 187 (2016) 281–290.
- [44] L.P. Wang, T.T. Huang, G.P. Yang, C.Y. Lu, F.L. Dong, Y.L. Li, W.S. Guan, The precursor-guided hydrothermal synthesis of CuBi₂O₄/WO₃ heterostructure with enhanced photoactivity under simulated solar light irradiation and mechanism insight, *J. Hazard. Mater.*, 381 (2020) 120956–120967.
- [45] L.P. Wang, G.P. Yang, D. Wang, C.Y. Lu, W.S. Guan, Y.L. Li, J. Deng, J. Crittenden, Fabrication of the flower-flake-like CuBi₂O₄/Bi₂WO₆ heterostructure as efficient visible-light driven photocatalysts: performance, kinetics and mechanism insight, *Appl. Surf. Sci.*, 495 (2019) 143521–143532.
- [46] F. Guo, M.Y. Li, H.J. Ren, X.L. Huang, K.K. Shu, W.L. Shi, C.Y. Lu, Facile bottom-up preparation of Cl-doped porous g-C₃N₄ nanosheets for enhanced photocatalytic degradation of tetracycline under visible light, *Sep. Purif. Technol.*, 228 (2019) 115770–115776.